Experimental and Numerical Analysis of Turbulent Opposed Impinging Jets

Gheorghe Stan* and David A. Johnson†
University of Waterloo, Waterloo, Ontario N2L 3G1, Canada

A fundamental study of two turbulent, directly opposed impinging jets in a stagnant ambient fluid, unconfined or uninfluenced by far-field walls, is presented. By experimental investigation and numerical modeling the fundamental characteristics of direct impingement of two turbulent axisymmetric round jets under seven different geometrical and flow-rate configurations ($L^* = L/d = \{5, 10, 20\}$, where L is nozzle to nozzle separation distance and d is nozzle diameter, and $Re = \rho U_0 d/\mu = \{1500, 4500, 7500, 11000\}$, where ρ is fluid density, μ is dynamic viscosity of fluid, and U_0 is average initial velocity of fluid) are discussed. Flow visualization and velocity measurements performed using various laser-based techniques have revealed the effects of Reynolds number Re and dimensionless nozzle to nozzle separation L^* on the complex flow structure. Similarity analysis of the initial freejet development and developing radial jet found $Re = 11 \times 10^3$ and $L^* = 20$ as the only case where the freejets exhibit a self-preserving development. However, the jets show significant growth with axial and radial distance for $Re = 7.5 \times 10^3$ and $L^* = 20$. All other experimental cases show little or no axial growth as a result of shorter development length. When used to simulate the present flow, the standard k-ε turbulence model showed little disagreement between computed and experimental mean velocities and poor predictions as far as the jet growth rates are concerned.

Introduction

TURBULENCE is one of the key phenomena in fluid dynamics. A major challenge in propulsion and mixing design is to provide the theory with highly accurate experimental data and rigorous turbulence models used in computational fluid dynamics (CFD) simulations. Jet-to-jet impingement is an engineering field that pertains to the research, development, and design of propulsion systems and various systems demanding a dynamic mixing of two or several jet flows in order to achieve their intended purpose. The system may be a side dump combustor of a vertical short takeoff and landing aircraft, a combustion chamber of an internal combustion engine, the environmental control system of a civilian airplane, the mix head for reaction injection molding (RIM), etc., which are of great industrial significance. In such configurations the mixing or combustion processes take place within the impingement region of the jets; therefore, the flow must maintain certain conditions to ensure the best efficiency and stability.

A quantitative description of mixing requires understanding of the fundamental processes that govern formation and evolution of jet-to-jet impingement structures. Even the simplest case of jet-to-jet impingement that undergoes a reaction can be regarded as a combination of four nonlinear, coupled, spatially, and temporally distributed processes: convection, stretching, diffusion and pressure interaction; chemical reaction or phase transform takes place instantaneously within the impingement region or follows the impingement process. When mixing is inadequate, desired reactions are slowed and even stopped before reaction is complete.

The jet-to-jet impingement configuration has usually been studied in the context of a particular application such as the side dump combustor[1] or the mix head for RIM,[2] where the two opposed impinging jets are wall-bounded and the interaction between an inner layer and an outer boundary layer is crucial; some fundamental aspects of that complex flow have never been clearly discussed. Moreover the traditional approach is guided mainly by the mirror image concept (MIC).[3] The concept indicates that the impinging of two jets separated by a distance L is theoretically equivalent to a single jet impinging on a flat plate at a distance $L/2$ downstream.

Previous free opposed planar impinging jet experiments reported in Denshchikov et al.[4,5] using flow visualization and laser Doppler anemometry (LDA) indicated an oscillation of the interface between the jets for some nozzle width/separation parameters. Ogawa and Maki[6] performed studies on two opposed axisymmetric turbulent jets mainly concerning body influences on the jet axis. In this study observations similar to those occurring in a jet impinging on a flat plate are commented.

In a similar study Ogawa and Maki[7] tried to establish the impact position of the two opposed jets and the magnitude of the "turbulent component" in the jet center when grids were used to generate the turbulent field. They found that the impact position of two turbulent opposed jets varies with the magnitude of turbulence of one side of the jet.

Shevtsov and Galin[8] examined the effect of flowrate fluctuations on the turbulence characteristics of countercurrent coaxial jets. The experiments involved two opposed planar jets separated by 20 nozzle heights. The results showed that the flow differs substantially from the structure of a jet impinging onto a flat plate located at a distance $L/2$ from the plane of discharge. The fluctuations in velocity were strongly displaced toward the low-frequency domain (0–40 Hz) with fluctuation amplitudes higher than those found for a jet impinging on a flat plate.

Some other studies of opposed impinging jets pertain to combustion and flame investigations,[9] which make separation and assessment of the nonreacting opposed jet flowfield difficult.

The motivation for the current work is the observation that understanding the fundamental characteristics associated with jet-to-jet impingement dynamics is essential in treating its derivative applications. Understanding the mechanism governing the turbulence structure and the instabilities associated with jet-to-jet impingement dynamics in an unconfined case is essential for determining mixing and entrainment characteristics present within more complex configurations. Consequently, this study starts with the general configuration of two opposed impinging jets in an initially stagnant large ambient fluid volume with wall boundaries at large distances.

The approach, followed both experimentally and computationally, is termed the free radial jet concept. According to this theory, the two opposed jets initially separated by a distance L impinge on each other at a station situated at about $L/2$ downstream and spread out radially creating a three-dimensional free radial jet (Fig. 1).
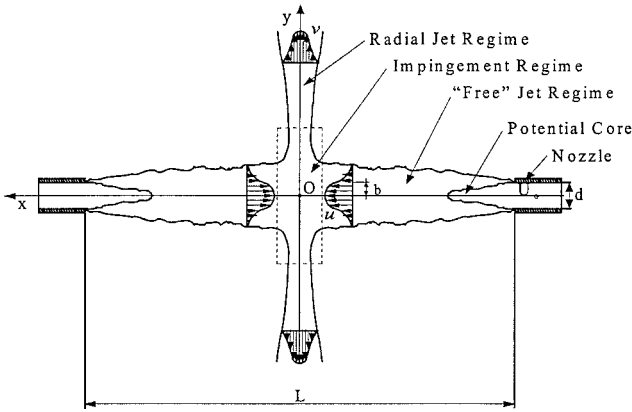
Fig. 1   Opposed impinging jets: free radial jet concept.

Fig. 2   Overall sketch of the flow system (not to scale): 1, submersible pump; 2, reservoir; 3, recycle valve; 4, flow control valve; 5, flow meter; 6, feeding line; 7, main tank; 8, opposed nozzles; 9, overflow valve; and 10, return line.
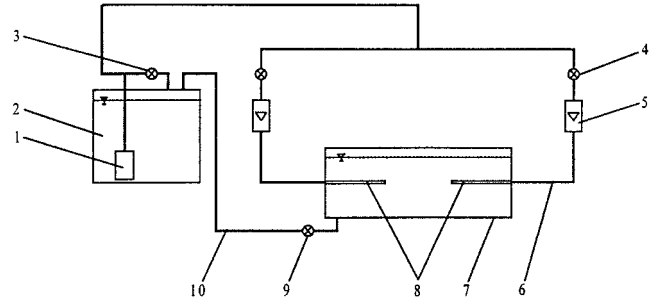
Experiment

Apparatus

Two identical aluminum round nozzles of inside diameter $d = 12.7$ mm were manufactured long enough to ensure a fully developed flow at their outlets (nozzle length $\gg 10 \cdot d$). To avoid exterior perturbations and wall effects, the two nozzles were isolated within a large tank (length × width × height = $1193 \times 584 \times 584$ mm) at a distance L apart. The spacing parameter $L^* = L/d$ was controlled by changing the length of the nozzles. An overflow at the liquid surface far from the jet area and a return valve in the tank bottom far from the jets controlled the fluid level, which was observed to remain steady. The results presented here utilize water [$\rho = 998$ kg/m^3, $\mu = 1.0 \times 10^{-3}$ kg/(m·s)] as the working fluid. Fluid was supplied to the nozzles at the same volumetric flow rates Q through a centrifugal submersible pump.

In this study the direct impingement of unconfined axisymmetric jets was examined using qualitative flow visualization methods such as laser-induced fluorescence (LIF), and quantitative velocity measurements were obtained using LDA and particle image velocimetry (PIV). Although the phenomena described in the present study are three-dimensional and time-dependent, a two-dimensional approach is followed here. Thus, the results provided are the output of LDA measurements in the horizontal plane xy for u and the vertical plane xz for v velocity components. Corresponding to the LDA results are the PIV measurements or numerically obtained u and v velocity components within the horizontal xy plane only. Four sets of flow-rate experiments were conducted for each nozzle-to-nozzle spacing parameter $L^* = \{20, 10, 5\}$. The Reynolds number of the respective flows is the product of the wetted diameter d and the associated volumetric flow rate of the nozzle, which gives the initial average velocity U_0: $Re = U_0 d/\nu = 4\rho Q/\pi \mu d$.

The three flow configurations $L^* = \{20, 10, 5\}$ used to assess the jet-to-jet impingement concept correspond to $Re = \{1.5 \times 10^3, 4.5 \times 10^3, 7.5 \times 10^3, 11 \times 10^3\}$. The overall arrangement of the opposing jet system is shown in Fig. 2.

Flow Visualization

The LIF technique was used to visualize the flowfield created within the imaginary horizontal plane containing the centerline of the two nozzles. Fluorescein dye was injected far upstream into the flow of one of the two nozzles in order to obtain uniform distribution of dye concentration and to avoid disturbing the flow. When the dye was excited by an argon ion laser light sheet, the flowfield generated by the opposed impinging jets was revealed and recorded by a video camera placed normal to the laser sheet.

LDA

Axial u and vertical (radial) v velocity components were obtained at previously determined locations using a conventional two-component dual-beam [consists of a 500-mW argon ion laser, optics, two photomultipliers, two counterprocessors, a frequency shifter, and a computer and interfacing hardware] LDA operating in forward scatter mode. Reviews of the theory and methods are provided in Refs. 10 and 11. For these measurements the laser and LDA op-

tics were mounted on a computer-controlled three-axis traversing stage so that accurate displacements could be achieved. In this configuration the measurement volume was approximately 1.1009 mm long and 0.06359 mm in diameter in one direction. At each measurement location 40,960 velocity measurements were obtained at a constant sampling frequency of 250 Hz to minimize bias. Data from the counterprocessor were transferred to a computer for storage, processing, and subsequent analysis. LDA measurements were obtained for the case corresponding to $Re = 11 \times 10^3$ and $L^* = 20$. Throughout all of the experiments, natural seeding of water has been found sufficient to obtain a data rate of 11.5–18.5 kHz.

PIV

Because of the high data density and to verify its applicability to such flow configurations (i.e., in comparison with the LDA approach), a PIV system was used to obtain the velocity fields for all model configurations presented. The system used in these experiments was a Dantec FlowMap PIV 2100 including the following components: a dual-cavity Nd:YAG laser with the associated light-sheet optics, a charge-coupled device camera, a programmable time delay and sequence generator, computer and image acquisition/processing software. The 532-nm laser beam was spread in one dimension to a thick (2–3-mm) light sheet using a cylindrical lens. Pulse separations of 1.5–10.5 ms were used depending on the following parameters: velocity being measured (Reynolds number) and particle size and type (material). The seeding particles were neutrally buoyant (particle density $\rho_p = 0.94$ g/cm^3) polypropylene spheres (53–250 μm) at a seeding density of approximately 20–40 particles in a 64×64 pixel sampling window. An 8-bit Kodak Megaplus ES 1.0 camera with 1008×1018 pixel array was focused to a field of view of 90.2×91.1 mm (scaling 9.946 pixels/mm). In these experiments, as a result of the relatively high number of cases studied and computer storage limitations, 250 image pairs were stored, excepting the case common to LDA measurements where 1000 image pairs were recorded. Cross correlations of image pairs and range and peak validations as part of the initial processing of the acquired data were performed using Dantec FlowManager software. Reviews of the theory and methods are provided in Refs. 11–13.

Numerical Computation

A numerical simulation of the opposed impinging jets flow was performed using a CFD code (TASCflow).[14] In TASCflow time-averaged equations are solved. Therefore, the conservation equations for an incompressible, Newtonian, isothermal flow can be written as follows.[14]

Continuity:

$$\frac{\partial \overline{u_i}}{\partial \overline{x_i}} = 0 \qquad (1)$$

Momentum:

$$\rho \frac{\partial \overline{u_i}}{\partial t} + \rho \frac{\partial (\overline{u_j u_i})}{\partial x_j} = -\frac{\partial \bar{p}}{\partial x_i} + \frac{\partial}{\partial x_j}\left(\overline{\tau_{ij}} - \rho \overline{u_i' u_j'}\right) + \overline{S_{ui}} \qquad (2)$$

where $\overline{u_i}, \overline{u_j}$ are spatial mean velocity vectors; u_i', u_j' are the fluctuating components of instantaneous u_i, u_j velocity vectors; and x_i, x_j are spatial coordinates (in tensor notation).

$$\overline{\tau}_{ij} = \mu D_{ij} = \mu \left(\frac{\partial \overline{u_i}}{\partial x_j} + \frac{\partial \overline{u_j}}{\partial x_i} \right) \tag{3}$$

is the mean viscous stress tensor and $\overline{S}_{ui}$ are additional source terms. D_{ij} is the viscous stress tensor.

A standard k-ε model was used because of its better performance within the impingement region,[11] which constitutes the most important zone of interest in this work. This model assumes that the turbulent viscosity is isotropic; therefore, the ratio between Reynolds stress ($-\rho \overline{u_i' u_j'}$) and mean strain rate is the same in all directions. The standard k-ε model assuming steady state has been previously utilized[1] in confining cases despite the unsteadiness of the flowfield. The limitations inherent in the use of this approach will be discussed in a subsequent section.

The computational domain was modeled by considering the 1:1 scale dimensions of the tank and the associated nozzles used in the experiments. TASCflow employs the finite control volume method to discretize the computational domain into a grid. The upwind differencing scheme was used to integrate the preceding governing equations over each control volume to yield a discretized system of algebraic equations. The final three-dimensional mesh used in simulations (Fig. 3) was obtained through a grid-refinement procedure and consisted of 123,008 cells (87×65 vertices in the symmetry plane). A symmetry boundary condition was applied to the computational domain cross-section symmetry plane containing the axial cross sections of the two nozzles and the cross section of the parallelepiped between the nozzle outlets. The no-slip condition ($u = v = 0$ [m/s]) was the boundary condition applied at the tank and nozzle side walls. Because the flow near the wall is of little interest in the present study, the wall boundary condition appears as a weak boundary condition in this simulation. Finally, the side and the top planes of the parallelepiped domain were modeled as opening boundary conditions, which allow for fluid entrainment from the surrounding ambient fluid.

The complex and unsteady character of the present problem made it difficult to obtain a converged solution. Several steps were required in the convergence procedure: manipulation of the boundary conditions, variation in the turbulence intensity and length scale, variation of the time step, and following a step-to-step convergence approach (i.e., running the code a few time steps, analyzing the evolution of the residuals, changing some of the preceding parameters and running it again). Therefore a representation of the degree of convergence would be inappropriate. In general the time steps used in these simulations fall in the interval $t \in [1.25, 0.1]$ [s] for $Re \in [1.5 \times 10^3, 11 \times 10^3]$ and $L^* = 20$. In all studied cases the iterative linear solver (using multigrid acceleration) attempts to reduce the

rms residuals of all of the momentum and mass equations as well as residuals of the turbulent kinetic energy and dissipation of turbulent kinetic energy equations down to a point where a maximum residual of 10^{-4} has been reached. Given the preceding convergence path, a total number of 105–146 combined iterations (time steps) was needed by the solver to reach the value of the maximum residual allowed. The number of iterations was observed to be a function of several variables involved such as Reynolds number, time-step value, eddy length scale, etc.

Measurement and Computational Errors

Using the rss method,[15] the error in calculation of the Reynolds number reported here was $\pm 4\%$. LDA velocity measurements are subject to errors in the location of the measurement control volume, gradient broadening, and electronic noise giving a total uncertainty in the mean velocities of 2–3% for the regions close to the nozzle exit plane and about 13% for measurements taken within the unsteady impingement region.[11] Calculation of the local mean velocity value based on 40,960 individual velocity measurements gave a random error below 0.5% (Ref. 16).

For the PIV measurements the particles cover approximately six pixels and therefore meet the minimum criterion for centroid location. Random error due to irregular particles, electronic noise, etc. is shown to be small (<0.1 pixel) by Prasad et al.[17] using larger particles and electronic timing errors are estimated to be small. These errors provide an error estimate of less than ± 1 pixel giving a positional error of less than 1%. These values (sub pixel positional accuracy and correspondingly small velocity errors) are in good agreement with Guezennec and Kiritsis.[18] The errors inherent in PIV velocity measurements are estimated to be of the order of 1%.[19]

Mesh refinement was the principal method of controlling the discretization errors when using TASCFlow to simulate the present flow. Overall, in all cases studied, the average percent difference in mean velocity between the coarse and finer grids was about 3.5%.

Results; Comments

Although CFD is able to provide three-dimensional data values, directional limitations imposed by the measurement equipment have led to confining the discussion of the overall flow field to the two-dimensional horizontal symmetry plane containing the centerline of the two jets.

Visual Observations

Figures 4a–4c represent typical flow visualization images collected for each of the four different flow rates $Re \in [11 \times 10^3, 7.5 \times 10^3, 4.5 \times 10^3, 1.5 \times 10^3]$ and correspond to the three jet configurations $L^* = \{20, 10, 5\}$.

In general, for all Reynolds number and geometrical configurations examined, the flow visualization study showed the formation of a composite flowfield characterized by the following distinct regions (Fig. 4): a potential core, a developing jet region (i.e., freejet region), an impingement region, and a free radial jet region. The structure (composition) of this complex flowfield is observed to be independent of Reynolds number and nozzle-to-nozzle spacing for the range of $Re \in [4.5 \times 10^3, 11 \times 10^3]$ and $L^* \in [5, 20]$. These observations confirm the free radial jet approach followed in this research.

No recirculation phenomena were observed within the impingement region or in the flowfield close to the jets for any Reynolds number or L^* in contrast to observations of confined impinging jets.[1] The flowfield contained within the impingement zone and a relatively large area surrounding it is significantly altered. The observed instantaneous impingement flowfield or the radial jet is not axisymmetric, nor stable and is highly unsteady. With only one jet dyed with fluorescent dye, a strong interaction was observed between the jet fields with the formation of small toroidal vortices at the periphery of the radial jet caused by the oscillation and movement of the impingement surface. The impingement surface created at the point of the jets impact is better defined and smoother as the Reynolds number and L^* decrease (Fig. 4). For all configurations the dyed jet is seen to exit the nozzle having a smooth cylindrical surface until small-amplitude waves appear on the jet boundary
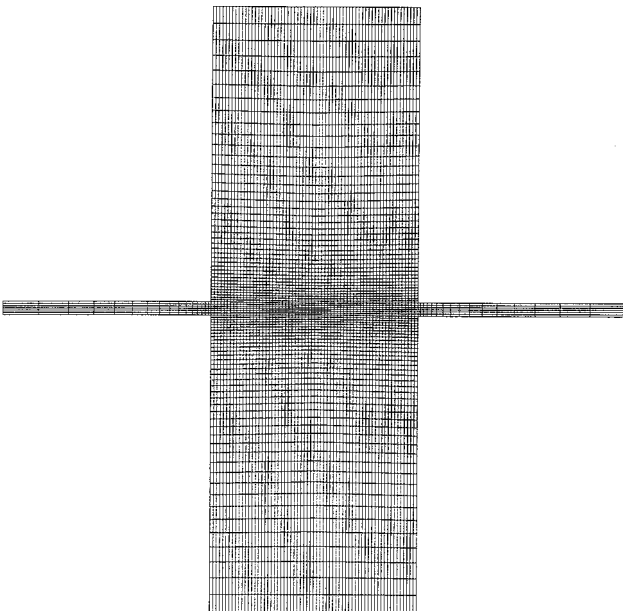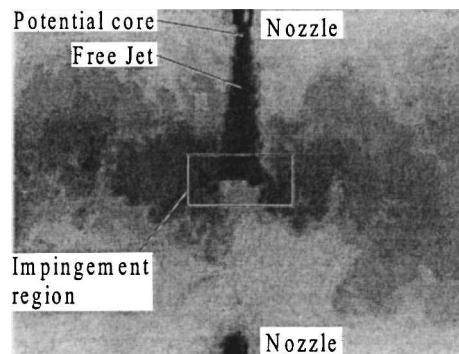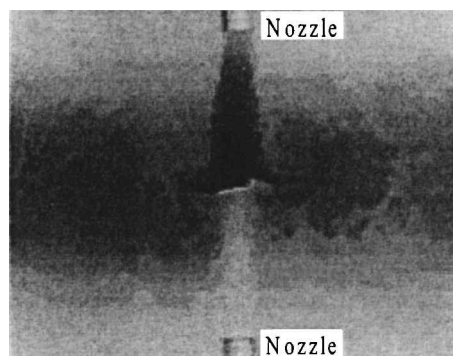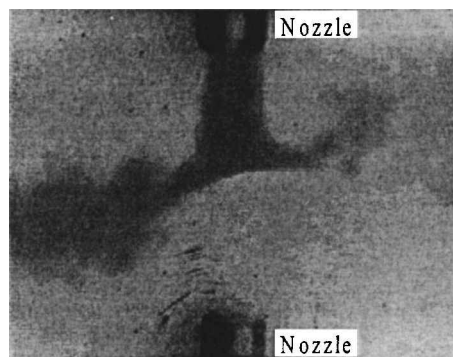

Fig. 3   Computational mesh: horizontal symmetry (XY) plane.

a) $L^* = 20$

b) $L^* = 10$

c) $L^* = 5$

Fig. 4   Turbulent opposed impinging jets: horizontal XY plane (LIF technique $L^* = L/d$, $Re = 11 \times 10^3$).

layer as a result of the entrainment process and shear layer instabilities. This phenomenon becomes more clearly visible when the Reynolds number and nozzle separation increase (Fig. 4). However, a clear relationship between the entrainment process and the impingement region area cannot be estimated from flow visualization images alone.

At the point of impingement (the stagnation point), the flow turns in the radial direction, and clear evidence exists of interface oscillation at the periphery of the radial jet in a plane perpendicular to the nozzle centerline. Also, there is evidence of oscillation of the entire impingement region along the nozzle centerline in the vicinity of the stagnation point. Using sequences of several images digitally separated from the flow visualization recordings, an estimation of the frequencies of oscillation was attempted. When examined on a frame-by-frame basis at 30 frames/s, the images revealed nonrepeatable and irregular oscillations in the low range of the frequency domain (1–20 Hz), as was also found by Shevtsov and Galin.[8] The frequency associated with the radial jet periphery f_r was observed to be higher than the translational oscillation of impingement region f_i. They both depend on Re and L^* in the sense that at higher Reynolds number and smaller L^* the oscillation frequencies are higher. Even though these oscillations were observed belonging to a restrictive frequency range, a definitive consistent measure of these frequencies could not be obtained.
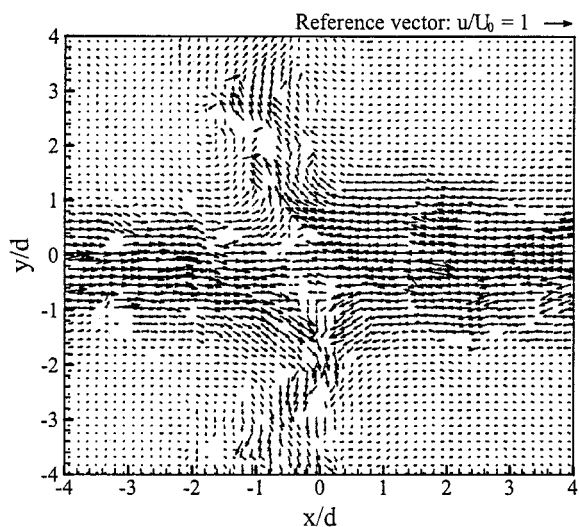
Mean Velocities

This section contains the analysis of the experimental data and simulated mean velocity results. Because the axisymmetric assumption has proven to be valid on average,[11] the correspondence between LDA and PIV measurement planes (xz and xy, respectively) is acceptable.

An examination of the ensemble-averaged velocity components at seven locations representing half of the velocity profile at $x = 125$ mm ($L^* = 20$, $Re = 11 \times 10^3$) away from the geometrical impingement point and for several sizes of the data block (i.e., 1000, 10,000, 20,000, 30,000, and 40,960) have revealed that at least 30,000 samples would be necessary to acquire a good accuracy in the full analysis.[11] Because this involves almost the same computational effort as the entire data set would, the complete sample size (i.e., 40,960 samples) was used in all calculations. Similarly, 250 image pairs were determined to provide reasonable accuracy when the PIV technique was employed.[11]

To evaluate the balance of the two initial jets and the entrainment level, several LDA and PIV volumetric flow rates were calculated for both jets at different x measurement stations before impingement and y sections after impingement. Integrating across the longitudinal velocity profiles associated with the two opposed nozzle outlets (i.e., 2 mm away from the nozzle) and configuration $L^* = 20$, $Re = 11 \times 10^3$, insignificant differences (0.18–0.9%) between the corresponding outlet flow rates and the initially measured flow rates were determined.[11] An analysis of the entrainment level has revealed an increase of the radial jet flow rate up to 4–5 times the magnitude of the initial axial flow rate.[11]

Although LDA and CFD results were obtained for the entire flowfield between the jets, the PIV field of view was limited to 8 diameters square, and all results are presented to this scale. Initial analysis of the instantaneously measured velocities showed that the overall flow under investigation is partially/locally stationary; therefore, the signal can be decomposed according to Reynolds decomposition into mean and fluctuating components. This assumption applies well to the signal recorded at locations situated closer to the axial and radial symmetry axes of the flow and for the u component. Larger variations about the measured mean longitudinal and radial velocities are found for locations at the periphery of the impingement area and in the impingement region. The measurement points surrounding the stagnation point and covering an approximately circular region of diameter $1d$–$1.5d$ are an exception to this rule. Although on average the impingement region is a surface and its position coincides with the geometrical symmetry plane of the two nozzles and the centerline of the radial jet, instantaneous vector plots show significant alterations of the overall flowfield (Fig. 5). The instantaneous velocity vector plot sample in Fig. 5 clearly shows the instantaneous radial jet created and the asymmetry of the flowfield as a result of the impact of the two jets. By averaging multiple

Fig. 5   Turbulent opposed impinging jets: instantaneous vector plot ($Re = 11 \times 10^3$, $L^* = 20$, PIV).
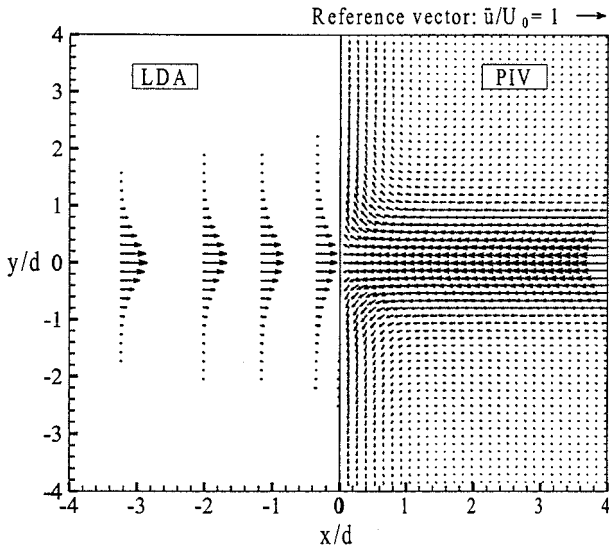
Fig. 6   Turbulent opposed impinging jets: mean velocity vector plot ($Re = 11 \times 10^3, L^* = 20$, LDA, PIV).
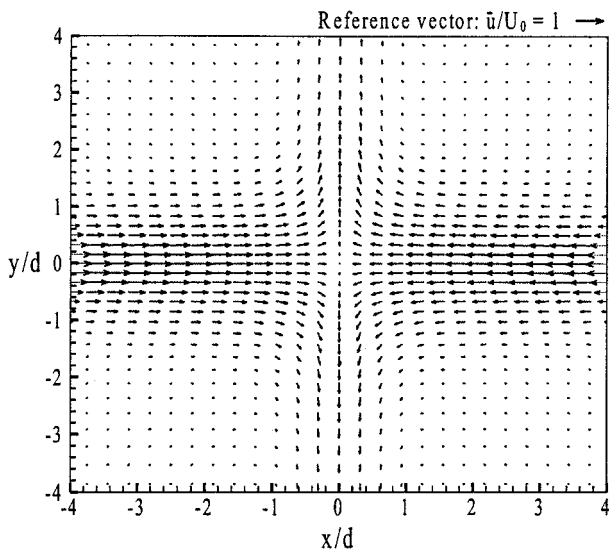

Fig. 7   Turbulent opposed impinging jets: mean velocity vector plot ($Re = 11 \times 10^3, L^* = 20$, CFD).

instantaneous vector plots, a mean velocity vector plot similar to that in Fig. 6 can be obtained. This result would therefore imply the existence of bidirectional oscillations of the impingement region about a symmetry plane situated at $L/2$ downstream of the nozzles and about the centerline of the two jets and variation in the associated entrainment rates.

Mean Velocity Vector Plots

Mean velocity vector plots obtained by mapping the LDA individual mean velocities and PIV and CFD data, for the same configuration case $Re = 11 \times 10^3$ and $L^* = 20$, are shown separately for clarity (Figs. 6 and 7). The x and y coordinates are normalized by nozzle diameter d and $\bar{u}$ and $\bar{v}$ by U_0 making comparisons between the two experimental techniques (LDA, PIV) and the CFD simulations possible. Both LDA and PIV mean velocity vector plots revealed symmetric distributions for the individual jets with respect to the jet axis and the geometric impingement point (Fig. 6). In addition, the PIV mean velocity vector plot provides a clear picture of the symmetric development of the radial jet about the orthogonal axes intersecting at the geometric impingement point.[11] It can be seen that these profiles become Gaussian in shape as they advance toward the impingement region (stagnation point). This is analogous to the behavior expected during evolution of a free jet.[20] Similar
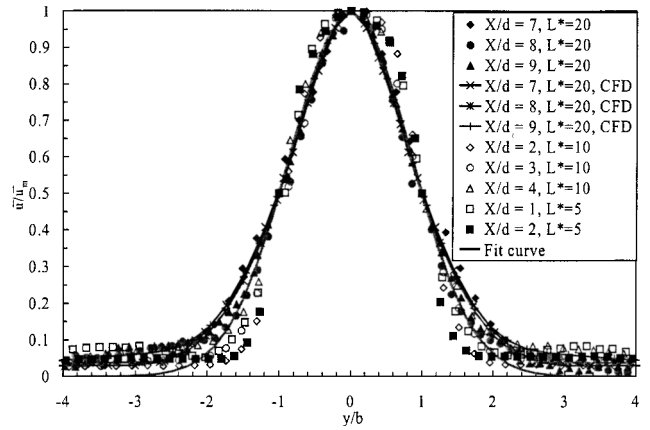

Fig. 8   Axial jet: mean longitudinal velocity distributions. PIV and CFD data: verifying the approach to self-similarity [fit curve = Reichardt momentum distribution in a freejet (4), X/d measured from nozzle exit plane].

comments can be made concerning the CFD generated mean velocity vector plot shown in Fig. 7. Although all vector plots show entrainment surrounding the two impinging jets, because of its very small magnitude (approximately 0.1–1 cm/s for $Re = 11 \times 10^3$) in comparison with that of the initial jets (1 m/s) and the radial jet (0.3 m/s) it has little influence on the jets' behavior. This observation confirms the steady condition of the fluid far from the jets (out of a $254 \times 100 \times 100$ mm control volume) and the unconfined assumption with regard to walls, overflow, and return line influences on the jet-to-jet impingement dynamics.

Similarity Analysis

Developing Free Jet

As shown in Ref. 11, both jets issue from the nozzles with a fully developed turbulent velocity profile. Up to the impingement region the magnitude of the mean longitudinal velocity component $\bar{u}$ of the two opposed jets is significantly larger than the mean transverse velocity $\bar{v}$. Considering the two initial jets to develop similarly with respect to the impingement region, a single jet development and the radial jet structure created as a consequence of the jet-to-jet impingement are discussed.

Figure 8 provides information regarding the distribution of mean longitudinal velocity across one of the two axial jets. The transverse coordinate y was normalized by the half-width of the jet b corresponding to the location where the velocity is one-half of the maximum velocity within that measurement section while the mean longitudinal velocity was normalized by the maximum mean velocity $\bar{u}_m$ within that section.

Figure 8 shows that self-similarity in the mean longitudinal velocity profile occurs by $X/d = 8$ (where $X = L/2 - x$ and is measured from the nozzle exit plane) of a possible $10d$ before the geometric center (measured from the exit plane of the nozzle) for $Re = 11 \times 10^3$ and $L^* = 20$. Previous studies[21] indicate that for this Reynolds-number range a fully developed jet exit condition will become similar much more rapidly than a uniform exit profile. No self-similar velocity profiles were found experimentally for $L^* = 20$ and $Re < 11 \times 10^3$. For nozzle-to-nozzle separations smaller than $20d$ and any of the Reynolds numbers studied, the experimental velocity profiles do not exhibit self-similarity in the range of X/d considered.[11] Regardless of the Reynolds number or L^*, all data collapse about the Reichardt distribution of momentum in a plane or axisymmetric free jet.[22] In this case the Reichardt Gaussian distribution over the width of the jet can be represented as

$$\bar{u} = \bar{u}_m \exp{-A(y/b)^2} \qquad (4)$$

where $A = \ell n 2$ is a constant largely unaffected by the Reynolds number or L^*. The self-preserving behavior was evaluated with regard to plot-to-plot match and not in comparison to a Reichardt distribution in a freejet. Reichardt momentum distribution in a free jet does suggest a general velocity profile trend in the opposed

impinging jets case, but matching this curve is not a self-similarity requirement.

The presence of the adverse pressure gradient within the impingement region deflects the jet in the radial direction, as can be seen in Fig. 6, but has little influence upstream of the impingement region.

Existing literature[23] states that for $X/d > 70$ the turbulent quantities would become self-preserving for freejet flow, a necessary condition for a self-preserving state. The relative longitudinal turbulence intensity ($u_{rms}/\bar{u}_m$) profiles never exhibit self-similarity for the range of X/d or Re and L^* studied. Although the relative turbulence intensity magnitudes were usually about 20–30% within the jet boundary layer, maximum values are obtained within the region surrounding the centerline of the jet. At the same time unexpected high turbulence intensities (between 40 and 80%) were found as Re and L^* decrease and even on the jet axis itself as a result of both turbulence and the effects of unsteady oscillations.

Radial Jet

Downstream of the stagnation point in the radial direction, the average velocity field begins to develop a distinctive Gaussian shape as shown in Fig. 9a. The experimental radial velocity profiles match the Reichardt distribution well although they do not exhibit self-similar behavior for any of the control parameters (y/d, L^*, or Re). The numerically determined radial velocity profiles in the case $Re = 11 \times 10^3$ and $L^* = 20$ exhibit self-preserving behavior for all y/d studied and within $1d$ of the radial jet axis ($-1 < x/d < 1$), whereas the boundary region of the radial jet (the region outside $1d$ of the radial jet axis) becomes self-similar for $y/d > 2$. CFD results match the experimental data corresponding to the peak of the velocity profile for $Re = 11 \times 10^3$ and $y/d = 1$, whereas the entrainment part of this distribution is overpredicted. No agreement

is recorded in the cases associated with $Re = 1.5 \times 10^3$; given the unsteadiness of the impingement area this is not surprising.

It can be observed that both mean radial velocity and radial turbulent intensity exhibit maximum values in the vicinity of or on the radial jet axis, which is consistent with the results of Ref. 8. This is in contrast to the MIC, which would not allow a velocity or turbulence peak at the wall surface. On average the centerline of the radial jet becomes the line of symmetry for the opposed impinging jets, which coincides with the average impinging surface location. Whereas for $Re = 11 \times 10^3$ the highest relative turbulent intensity levels (about 60–80%) are concentrated about the centerline of the radial jet (Fig. 9b), a more uniform turbulent intensity (about 20%) toward the lower limit of the Reynolds number range is observed.

Jet Growth

In general, the jet growth rate is evaluated by the change in the half-width of the jet with b as a function of distance from nozzle exit. Thus, data obtained from similarity analysis were used to determine the jet growth variation associated with each Reynolds number and nozzle-to-nozzle separation distance.

As illustrated in Fig. 10a for the initial region within $5d$ downstream of the nozzle for the axial jet and $5d$ downstream of the stagnation point for the radial jet (Fig. 10b), all of the jets satisfy linear growth laws similar to those associated with freejet flows.[24] The general law of relative growth (b/d) variation as a function of the jet relative advancement (X/d or y/d) could be represented by

$$b/d = a_1(X/d) + a_2 \qquad (5)$$

where a_1 is the slope of the line and a_2 is an arbitrary constant. The values for a_1 and a_2 corresponding to both axial and radial jets are shown in Table 1.

The variation of the experimental axial jet growth rate is shown in Fig. 10a. The case $Re = 11 \times 10^3$ and $L^* = 20$ showed significant growth with axial distance. All other $Re = 11 \times 10^3$ experimental cases show little or no growth with axial distance as a result of shorter development length. As expected for a constant Reynolds number, the growth rate increases as L^* increases. Literature describing free plane turbulent jet behavior shows the existence of a "natural" variation of jet growth with respect to Reynolds number variation. For example Otugen and Namer[24] determined that the value of a_1 decreases with increasing Re and found $a_1 = 0.179$ for $Re = 1 \times 10^3$ and $a_1 = 0.098$ for $Re = 6 \times 10^3$ for a free plane turbulent jet. A similar variation of a_1 was determined for the present flow, and these values $a_1 = 0.1735$ ($Re = 7.5 \times 10^3$) and $a_1 = 0.097$ ($Re = 11 \times 10^3$) agree well with Otugen and Namer[24] and Schlichting.[22] A linear measurement of jet growth was not found for any flow conditions at $L^* = 5$ (Table 1). Because of the highly unstable and almost laminar character of the flow corresponding to $Re = 1.5 \times 10^3$ and regardless of the L^* value, no clear pattern emerges.

Similar behavior is exhibited by the average radial jet (Fig. 10b) created when the two opposed jets impinge on each other. The values of a_1 corresponding to the radial jet are provided in Table 1. As Reynolds number increases, the growth rate increases such that the maximum jet width would be achieved for $Re = 11 \times 10^3$ and
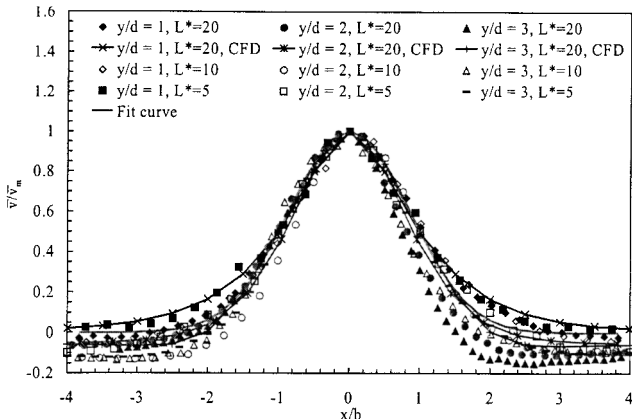

Fig. 9a   Radial jet: mean radial velocity distributions. PIV and CFD data: verifying the approach to self-similarity (fit curve = Reichardt momentum distribution in a freejet, y/d measured from axial jet axis, $Re = 11 \times 10^3$).
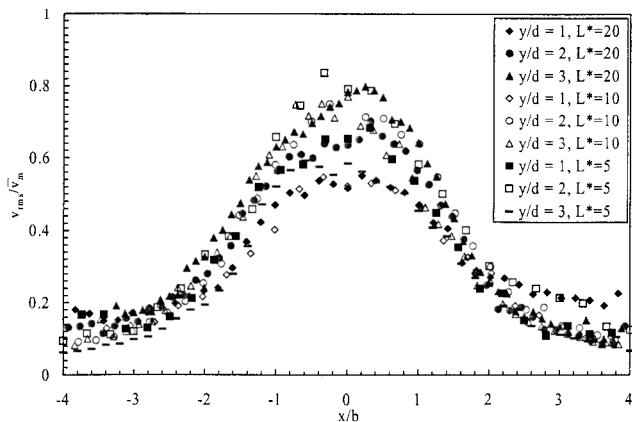

Fig. 9b   Radial jet: turbulent intensity distributions. PIV and CFD data.

Table 1   Axial and radial jets: parameters of the growth rate variation law

Jet flow			Axial			Radial		
Re	L^*		20	10	5	20	10	5
11×10^3	PIV	a_1	0.097	0.0055	0.010	0.172	0.148	0.077
		a_2	−0.078	0.527	0.457	−0.655	0.0403	0.167
	CFD	a_1	0.126	N/A	N/A	0.020	N/A	N/A
		a_2	−0.193	N/A	N/A	0.492	N/A	N/A
7.5×10^3	PIV	a_1	0.1735	0.0245	0.074	0.1575	0.0865	0.004
		a_2	−0.658	0.4555	0.45	0.441	0.2518	0.322
4.5×10^3	PIV	a_1	0.159	0.0605	−0.025	0.111	0.101	−0.048
		a_2	−0.333	0.3071	0.541	0.422	0.284	0.38
1.5×10^3	PIV	a_1	0.003	0.002	0.054	0.057	0.010	0.037
		a_2	0.518	0.351	0.305	0.187	0.319	0.046
	CFD	a_1	0.177	N/A	N/A	−0.0045	N/A	N/A
		a_2	−0.593	N/A	N/A	0.662	N/A	N/A
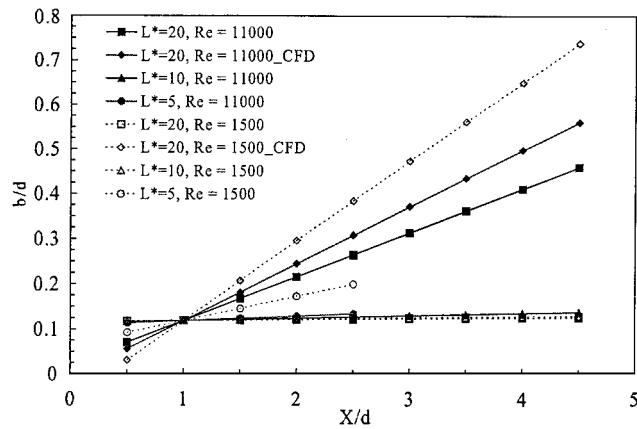
a) Axial jet
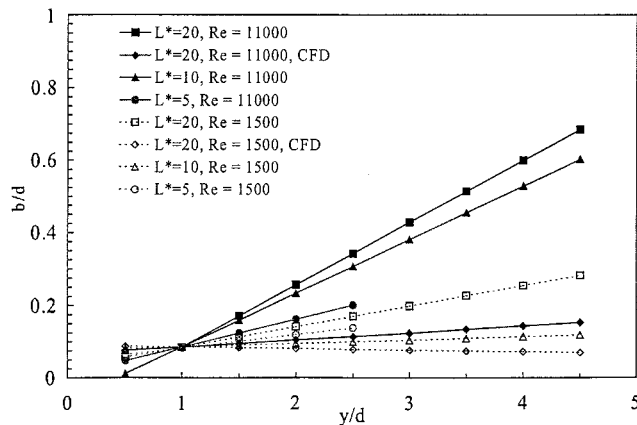
b) Radial jet

Fig. 10 Effect of Reynolds number and nozzle to nozzle separation L^* on the growth rate of the jet (PIV and CFD data; - - - -, suggested trend for visual purposes only).

$L^* = 20$; therefore, the jet spreads out faster or has higher fluctuation.

As far as the CFD solution is concerned, it predicts the evolution of a freejet flow but with different growth rates. It greatly overpredicts the growth rate of the axial jet, whereas the radial jet development is underpredicted.

Quantitative Oscillation Analysis

The velocity time series analysis for all cases obtained with the LDA did not reveal any single dominant frequencies. This is consistent with the flow visualization studies. Confined jet furnace model studies reported in Ref. 25 found time-dependent simulations to give a constant low frequency of oscillation while experimentally measured frequencies were nonconstant and varied by a factor of two about the computed value. Similar results of frequencies in the range of 5–6 to 10–12 Hz are reported in Ref. 8. The confining wall boundaries of these studies tend to stabilize the flow through flow recirculation although in the present study with no confinement no stable frequencies were found.

Conclusions

In this research several experimental and computational techniques have been employed in an attempt to clarify some of the fundamental aspects of the complex flow created in the impingement region of two turbulent opposed jets. The study was performed by combining qualitative examination of the flow through visualization with a classical analysis of measured and computed mean and turbulent velocity data. Several conclusions can be drawn:

1) For all Reynolds numbers and L^* studied, a composite flowfield consisting of a potential core, a developing jet region, an impingement region, and a developing free radial jet region was observed. Direct jet-to-jet impingement was observed for all cases studied in contrast to previously reported work.[4]

2) No significant recirculation flow was observed or measured in this quasi-unbounded configuration in contrast to studies confining the jets in a cavity. Flow visualization images and PIV instantaneous vector plots demonstrated that the instantaneous flowfield generated by the impingement of two coaxial opposed jets is not axisymmetric, nor stable, and is highly unsteady. On average the impingement region becomes a steady radial jet. The impingement surface created at the point of impact is better defined and smoother as Reynolds number and L^* decrease. The entrainment process becomes more clearly visible when Reynolds number and nozzle-to-nozzle separation increase.

3) Unlike the round freejet that maintains a self-preserving shape of mean velocity profiles at about 20 diameters downstream regardless of Reynolds number,[20] the opposed impinging jets become self-similar in the mean velocity at just 8 diameters downstream of the nozzles for $Re = 11 \times 10^3$ and $L^* = 20$, which is consistent with fully developed jet exit profiles in the Reynolds-number range.[21] Turbulence intensity profiles do not exhibit self-similarity for the range of X/d or Reynolds numbers and L^* studied. The high magnitude of the turbulence quantities measured within the impingement region (between 40 and 80%) are caused by the highly oscillatory behavior of the impinging jets.

4) Although for $Re = 11 \times 10^3$ and independent of L^* the mean radial velocity profiles match the Reichardt distribution well for freejets, none of them exhibits a completely self-similar behavior for any of the control parameters (i.e., y/d, L^*, or $Re = 11 \times 10^3$). CFD results match the experimental data corresponding to the top part of the velocity profiles for $Re = 11 \times 10^3$ and $y/d = 1$ well while they overpredict the base part of this distribution. This is consistent with the assumption of steady flow here and the assumption of isotropy that is the basis of the k–ε turbulence model.

5) Even though the flow at $Re = 7.5 \times 10^3$ does not exhibit self-similarity for L^* considered in this study, it provides the largest jet growth rate. This fact implies a higher rate of entrainment and therefore a better mixing of the axial and radial jet with the surrounding fluid. It can be also affirmed that in an opposed jet impingement configuration with $Re \in [1.5 \times 10^3, 7.5 \times 10^3]$ the rate of axial jet development (spreading) is about twice the development rate of a free planar jet for the same flow conditions. The jet growth increases with increasing L^* as would be expected in a developing jet. The impingement region with high streamline curvature and adverse pressure gradient may influence the jet growth in the radial direction.

6) Because of the unsteady nature of the jet interaction, no well-defined oscillation frequencies were obtained although there is significant energy in the low frequency range.

7) The steady CFD simulation using a standard k–ε turbulence model fails in the impingement region because of the implied steadiness and limitation in the k–ε model formulation.

References

[1]Liou, T.-M., and Wu, S.-M., "Turbulent Flows in a Model SDR Combustor," *Journal of Fluids Engineering*, No. 115, No. 3, 1993, pp. 468–476.

[2]Wood, P., Hrymak, A., Yeo, R., Johnson, D., and Tyagi, A., "Experimental and Computational Studies of the Fluid Mechanics in an Opposed Jet Mixing Head," *Physics of Fluids*, Vol. A, No. 3, 1991, pp. 1362–1372.

[3]Birkhoff, G., and Zarantonello, E., *Jets, Wakes and Cavities*, Vol. 2, Applied Mathematics and Mechanics, Academic Press, New York, 1957.

[4]Denshchikov, V. A., Kondrat'ev, V. N., and Romashov, A. N., "Interaction Between Two Opposed Jets," *Journal of Fluid Dynamics*, Vol. 6, No. 924, 1978, pp. 924–926.

[5]Denshchikov, V. A., Kondrat'ev, V. N., Romashov, A. N., and Chubarov, M., "Auto-Oscillations of Planar Colliding Jets," *Journal of Fluid Dynamics*, Vol. 3, No. 460, 1983, pp. 460–463.

[6]Ogawa, N., and Maki, K., "Studies on Opposed Turbulent Jets (Influences of a Body on the Axis of Opposed Turbulent Jets)," *Bulletin of the Japan Society of Mechanical Engineers*, Vol. 29, No. 255, 1986, pp. 2872–2877.

[7]Ogawa, N., and Maki, K., "Studies on Opposed Turbulent Jets (Impact Position and Turbulent Component in Jet Center)," *JSME International Journal*, Vol. 35, No. 2, 1992, pp. 205–211.

[8]Shevtsov, A. A., and Galin, N. M., "The Effect of Flowrate on the Turbulence Characteristics of Countercurrent Coaxial Jets," *Journal of Thermal Engineering*, Vol. 39, No. 6, 1992, pp. 332–335.

[9]Williams, F. A., "Progress in Knowledge of Flamelet Structure and Extinction," *Journal of Progress in Energy and Combustion Science*, Vol. 26, No. 4–6, 2000, pp. 657–682.

[10] Durst, F., Melling, A., and Whitelaw, J. H., *Principles and Practice of Laser-Doppler Anemometry*, 2nd ed., Academic Press, New York, 1981.

[11] Stan, G., "Fundamental Characteristics of Turbulent Opposed Impinging Jets," M.Sc. Thesis, Dept. of Mechanical Engineering, Univ. of Waterloo, Waterloo, ON, Canada, Sept. 2000; http:\\library.uwaterloo.ca\etd\ ethesis.html [cited 1 June 2001].

[12] Raffel, M., Willert, C., and Kompenhans, J., *Particle Image Velocimetry—A Practical Guide*, Springer-Verlag, Berlin, 1998.

[13] Dantec Measurement Technology Department, "FlowMap Particle Image Velocimetry Instrumentation. Installation User's Guide," Skovlunde, Denmark, Oct. 1998.

[14] "TASCFlow and CFX—Build: Theory Documentation," AEA Technology, Waterloo, ON, Canada, Nov. 1994.

[15] Moffat, R. J., "Describing the Uncertainties in Experimental Results," *Experimental Thermal and Fluid Science*, Vol. 1, No. 1, 1988, pp. 3–17.

[16] Pereira, J. C. F., and Sousa, J. M. M., "Experimental and Numerical Investigation of Flow Oscillations in a Rectangular Cavity," *Journal of Fluids Engineering*, No. 117, No. 1, 1995, pp. 68–74.

[17] Prasad, A. K., Adrian, R. J., Landreth, C. C., and Offutt, P. W., "Effect of Resolution on the Speed and Accuracy of Particle Image Velocimetry Interrogation," *Experiments in Fluids*, No. 13, 1992, pp. 105–116.

[18] Guezennec, Y. G., and Kiritsis, N., "Statistical Investigation of Errors in Particle Image Velocimetry," *Experiments in Fluids*, No. 10, No. 2–3, 1990, pp. 138–146.

[19] Westerweel, J., "Fundamentals of Digital Particle Image Velocimetry," *Measurement Science and Technology*, Vol. 8, No. 12, 1997, pp. 1379–1392.

[20] White, F. M., *Viscous Fluid Flow*, McGraw–Hill, New York, 1991, pp. 470–481.

[21] Ferdman, E., Otugen, M. V., and Kim, S., "Effect of Initial Velocity Profile on the Development of Round Jets," *Journal of Propulsion and Power*, Vol. 16, No. 4, 2000, pp. 676–686.

[22] Schlichting, H., *Boundary Layer Theory*, Series in Mechanical Engineering, 6th ed., McGraw–Hill, New York, 1968, pp. 729–757.

[23] Wygnanski, I., and Fiedler, H., "Some Measurements in the Self-Preserving Jet," *Journal of Fluid Mechanics*, Vol. 38, Pt. 3, 1969, pp. 577–612.

[24] Namer, I., and Otugen, M. V., "Velocity Measurements in a Plane Turbulent Air Jet at Moderate Reynolds Numbers," *Experiments in Fluids*, Vol. 6, No. 6, 1988, pp. 387–399.

[25] Quick, J. W., Gartshore, I. S., and Salcudean, M., "The Interaction of Opposing Jets," *Ninth Symposium on Turbulent Shear Flows*, Kyoto, Japan, Aug. 1993, pp. 6-4-1–6-4-6.

R. M. C. So
Associate Editor